

Packed bed thermal energy storage: A novel design methodology including quasi-dynamic boundary conditions and techno-economic optimization

Silvia Trevisan^{a,*}, Yousra Jemmal^b, Rafael Guedez^a, Björn Laumert^a

^a Department of Energy Technology, KTH Royal Institute of Technology, Brinellvägen 68, 100 44 Stockholm, Sweden

^b Department of R&D and Industrial Integration, Moroccan Agency for Sustainable Energy (MASEN), Complexe Zénith Rabat N°50, Rocade Sud Rabat-Casablanca Immeubles A-B-C-D, Souissi, Rabat, Morocco

ARTICLE INFO

Keywords:

Packed bed
Thermal energy storage
Design methodology
Levelized cost of storage
Multi-objective optimization

ABSTRACT

High temperature thermal energy storages are becoming more and more important as a key component in concentrating solar power plants. Packed bed storages represent an economically viable large scale energy storage solution. The present work deals with the analysis and optimization of a packed bed thermal energy storage. The influence of quasi-dynamic boundary conditions on the storage thermodynamic performance is evaluated. The Levelized Cost of Storage is innovatively applied to thermal energy storage design. A complete methodology to design packed bed thermal energy storage is proposed. In doing so, a comprehensive multi-objective optimization of an industrial scale packed bed is performed. The results show that quasi-dynamic boundary conditions lead to a reduction of around 5% of the storage thermal efficiency. Contrarily, the effect of the investigated design variables over the TES LCoS optimization is only slightly influenced by quasi-dynamic boundary conditions. Aspect ratio between 0.75 and 0.9 would maximize the storage thermal efficiency, while low preliminary efficiency around 0.47 would minimize the Levelized Cost of Storage. This work testifies that quasi-dynamic boundary conditions should be taken into considerations when optimizing thermal energy storage. The Levelized Cost of Storage could be also considered as a more reliable performance indicator for packed bed thermal energy storage, as it is less dependent on variable boundary conditions.

1. Introduction

The integration of thermal energy storage (TES) systems is key for the commercial viability of concentrating solar power (CSP) plants [1, 2]. The inherent flexibility, enabled by the TES is acknowledged to be the main competitive advantage against other intermittent renewable technologies, such as solar photovoltaic plants, which are much cheaper on the sole basis of the Levelized Costs of Electricity (LCoE). TES not only permits decoupling of the solar concentration and the electricity generation, but it also grants enough operational flexibility and dispatchability to the CSP plant enlarging its capacity factor. Packed bed TES systems using natural rocks as sensible storage material and air as main heat transfer fluid (HTF) have been shown to be especially suitable for the next generation of high-temperature CSP plants [3]. This technology can offer several advantages: (1) cheap and abundant storing material, (2) wide temperature range and high maximum temperature, (3) direct heat transfer between working HTF and storing material avoiding the need of an intermediate heat exchanger, (4) no chemical

instability, degradation and corrosion and (5) low safety concerns [4].

Although the packed bed TES is a rather simple concept, to further develop the technology and maximize its performance many design choices need to be assessed. Particularly, the TES behavior can be influenced by several geometrical, operational and thermo-physical parameters. Due to the high number of parameters, comprehensive experimental investigations are extremely expensive and time-consuming. Therefore, to assess the influence of all these factors, simulations, sensitivity analyses and single and multi-objective optimizations have been performed.

Sensitivity studies, in which parameters are varied in a systematic way in order to identify their influence on some performance indicators, are rather common in previous literature. These investigations assess also the robustness of the solution algorithm used to model the TES thermal behavior. Among sensitivity studies, Hänen et al. [5] investigated the temperature distribution along the TES together with the charge and discharge efficiencies, the capacity ratio and the thermal losses as function of the HTF mass flow rate, TES height, storing material and particle diameter. Zanganeh et al. [6] introduced a truncated

* Corresponding author.

E-mail address: trevisan@kth.se (S. Trevisan).

Nomenclature	
Abbreviations	
CAPEX	Capital expenditure [M\$]
CSP	Concentrated Solar Power
DNI	Direct Normal Irradiance [W/m ²]
HTF	Heat Transfer Fluid
KPI	Key Performance Indicators
LCoE	Levelized Cost of Electricity [\$/MWh _e]
LCoS	Levelized Cost of Storage [\$/MWh _e]
MOO	Multi-Objective Optimization
OPEX	Operational Cost [M\$]
PV	Photovoltaic
SM	Solar Multiple [-]
TES	Thermal Energy Storage
Symbols	
A	Cross-sectional area [m ²]
a_{in}	Convective heat transfer coefficients on the inside of the TES tank [W/(m ² ·K)]
a_{in}	Convective heat transfer coefficients on the outside of the TES tank [W/(m ² ·K)]
a_s	Packed bed surface to volume ratio [m ⁻¹]
c_{el}	Electricity cost [\$/kWh _e]
c_i	Specific cost [\$/m ³]
c_p	Specific heat [J/(kg·K)]
D	Storage diameter [m]
d_p	Particle diameter [m]
E	Energy [MWh]
E_{pump}	Pumping energy [MWh]
G	Mass flow rate per unit area [kg/(m ² ·s)]
h	Convective heat transfer coefficient [W/(m ² ·K)]
h^*	Corrected convective heat transfer coefficient [W/(m ² ·K)]
H	Storage height [m]
h_{RS}	Heat transfer coefficient for radiation solid to solid [W/(m ² ·K)]
h_{RV}	Heat transfer coefficient for radiation void to void [W/(m ² ·K)]
k	Thermal conductivity [W/(m·K)]
K	Solid and fluid thermal conductivity ratio
k_0	Thermal conductivity contribution due to conduction in each phase [W/(m·K)]
k_R	Thermal conductivity contribution due to radiation
\dot{m}	between solids [W/(m·K)]
n	Mass flow rate [kg/s]
N _{mat}	Number of contact points on a semispherical surface of a single pebble
N _{op}	Number of materials
N _{TES}	Number of operational years [y]
r	Number of storage units
T	Discount rate
t	Temperature [K]
TC	Time [s]
U _w	Thermocline [%]
V _i	Overall heat transfer coefficient [W/(m ² ·K)]
V _{TES}	Volume of materials [m ³]
x	Volume of the thermal energy storage [m ³]
	Length [m]
Greek symbols	
α	Aspect ratio
Δp	Pressure drop [Pa]
ΔT	Temperature difference [K]
ε	Void fraction
η_0	Preliminary sizing efficiency
η_{compr}	Air compressor efficiency
η_{cycle}	Thermal to electricity conversion efficiency
η_{th}	Thermal efficiency
μ	Fluid dynamic viscosity [Pa s]
ξ_R	Thermal emissivity
ρ	Density [kg/m ³]
σ	Stephan-Boltzmann constant [W/(m ² ·K ⁴)]
ϕ_t	Ratio fluid film effective thickness to particle diameter
Subscripts	
∞	Undisturbed environment
avg	Average
ch	Charge
DES	Design
disch	Discharge
eff	Effective
F	Fluid
in	Inlet
out	Outlet
ovr	Overall
S	Solid

conical TES geometry and analyzed the influence of the TES cone angle. González et al. [7] developed a thermo-elastic model of the TES unit, including the interaction between the filler material and the tank, to analyze the stresses on the TES tank. Bonanos et al. [8] performed a comprehensive parametric study on a TES model to predict the thermocline thickness using the Monte Carlo based Morris' screening method.

In contrast with sensitivity studies, optimization analyses are rare in previous literature. In optimization studies, some geometrical or operational parameters are considered as design variables and then a mathematical optimization algorithm is exploited to find an optimum design point. Single and multi-objectives studies are distinguished based on the number of performance indicators set as objectives. The large majority of single objective optimizations aimed at maximizing the TES thermodynamic efficiency. Torab et al. [9] exploited a monotonicity method to maximize the TES thermodynamic availability. The results showed that the total availability increases with smaller particle diameter and higher TES height. However, these design choices lead to lower ratio of total availability to air circulation energy. Ammar et al. [10]

investigated the maximum ratio between stored to air circulation energy by means of a direct search method, considering TES height, particle diameter and HTF flow rate as decision variables. Maaliou et al. [11] introduced some economic considerations, and maximized the net income, evaluated as the difference between the value of stored heat and the cost of the equipment and its operation. Modifying the collection time led to a maximum profile of the net income. The results showed also that an independent increase of TES diameter, height or particle size leads to a sharp increment of the net income, followed by a slow and gradual decrease. Lundgaard et al. [12] performed a density-based topology optimization for a 2D packed bed TES, optimizing the spatial distribution of two storage media (rocks and sand). The results showed that a relative increase of 46 % of the TES thermodynamic performance can be achieved.

In multi-objective optimizations (MOO), the TES thermal energy or exergetic efficiency are usually maximized while minimizing the TES capital expenditure (CAPEX). Choudhury et al. [13] optimized the total energy stored together with the cost per unit of energy stored. The optimal values of HTF flow rate and TES cross sectional area have been

shown as strongly dependent on the unit operating temperatures. White et al. [14] presented a combined optimization of TES CAPEX and second law efficiency for traditional packed beds and segmented storages. The results suggested that segmented packed beds might be particularly suitable for cold TES. Marti et al. [15] maximized the TES exergy efficiency while minimizing the material cost via a constrained MOO. The TES height, top and bottom radii, insulation thickness and particle diameter were considered as design variables. The results showed that a truncated conical shape with the smallest section at the top would lead to the highest exergy efficiency. However, a similar TES design might induce higher thermo-mechanical stresses and thermal ratcheting risk. The optimization identified a TES design with a cost about 81% lower than the one of the most efficient unit and a reduction of the exergy efficiency of less than 5%. Finally, Cárdenas et al. [16] presented the optimization of an utility-scale packed bed TES. The authors analyzed the effects of particle diameter, aspect ratio and storage mass on exergy efficiency and cost per unit of stored. The study showed that exergy losses were minimized when the aspect ratio was kept within 0.5 to 0.8. Additionally, it was reported that TES mass overrating leads to improved thermodynamic performance and a 50% oversizing permits minimal cost per unit of stored exergy.

Previous studies devoted to packed bed TES optimization suffer from two main limitations. Firstly, constant working conditions have been assumed for all simulated operational cycles, specifically constant HTF mass flow rate during the charging period. Secondly, only the TES thermal efficiency and the CAPEX have been set as objectives.

To start with, the assumption of constant working conditions is far from the real operation, particularly if the TES is installed in a CSP plant. The schematic layout of a representative CSP plant including a packed bed TES is shown in Fig. 1. During daylight, the generated thermal power in the receiver is variable, dependent on the DNI level and solar field optical efficiency. Contrarily, in order to maintain the power unit working conditions as close as possible to the design ones, a constant power is feed to the main heat exchanger of the power block. One of the main goals of CSP plants' control strategies is to maintain a constant receiver outlet temperature; in doing so, the HTF mass flow rate is controlled based on the incoming solar power. The TES acts as a buffer for the overall system and it receives a fluctuating thermal power input. In order to fill the first identified research gap, the present work aims at assessing the influence of quasi-dynamic boundary conditions on the thermal behavior of a large scale packed bed TES. Different HTF mass flow rate profiles are simulated during the charge period and the main thermodynamic performance is studied for several consecutive operational cycles. Thermocline thickness, TES overall efficiency, duration of the discharge period, and thermal energy output are identified as thermodynamic key performance indicators.

Secondly, the utilization of the CAPEX as the main economic indi-

cator provides only limited indications on the economic performance of the designed TES. Only few insights are derived on how or whether the initial investment can be recovered. Besides, no proper comparison among energy storage technologies can be on the sole basis of the CAPEX. To address this second limitation, in this work a simplified economic model is developed and the Levelized Cost of Storage (LCoS) concept is introduced and applied to packed bed TES. The LCoS has been recently proposed to evaluate the economic performance of energy storage and to permit comparison among storage technologies, renewable and traditional power generation systems [17]. The LCoS, analogously to the more conventional LCoE, refers to the discounted cost of electricity per unit of discharged electricity. Among previous related literature, Pawel [18] evaluated the LCoS for a PV power plant including batteries. Redox-flow batteries showed the lowest LCoS among the considered ones and the C-rate was identified as the most affecting parameter. Jülich [19] presented an analysis of the LCoS of four different ES technologies. The results showed that pumped hydroelectric storage achieves the lowest LCoS for both long and short-term electricity storage. Nonetheless, power to gas and adiabatic compressed-air energy storage showed potential to become cost competitive as short-term energy storage. Smallbone et al. [20] extended a similar analysis to pumped heat energy storage showing that they are cost-competitive with adiabatic compressed-air energy storage. Luerssen et al. [21] compared thermal energy storage and battery for cooling application coupled with PV systems on the basis of the LCoS. Schmidt et al. [22] evaluated the LCoS development for nine different technologies in twelve power systems in the time horizon 2015–2050. State-of-the-art works apply the LCoS mostly to electrical energy storages. In this work, a methodology to apply the LCoS to TES is presented. In doing so, a comprehensive methodology for packed bed TES design optimization is proposed. As part of the suggested methodology, and in order to seek for a more reliable packed bed TES optimization routine, different multi-objective optimizations have been performed under distinct quasi-dynamic working conditions to assess the optimal TES design. The considered objectives are to maximize the TES overall thermodynamic efficiency while minimizing LCoS and CAPEX. For these studies, particle diameter, TES aspect ratio ($\alpha = H/D$), number of TES tank, HTF mass flow rate during discharge, and preliminary sizing efficiency are considered as the main decision variables.

2. Modeling

2.1. Packed bed thermal energy storage model

Several previous studies have analyzed packed bed modeling strategies and its thermal behavior. In this work, a thermodynamic model of the axial flow packed bed TES, based on the established Schumann's

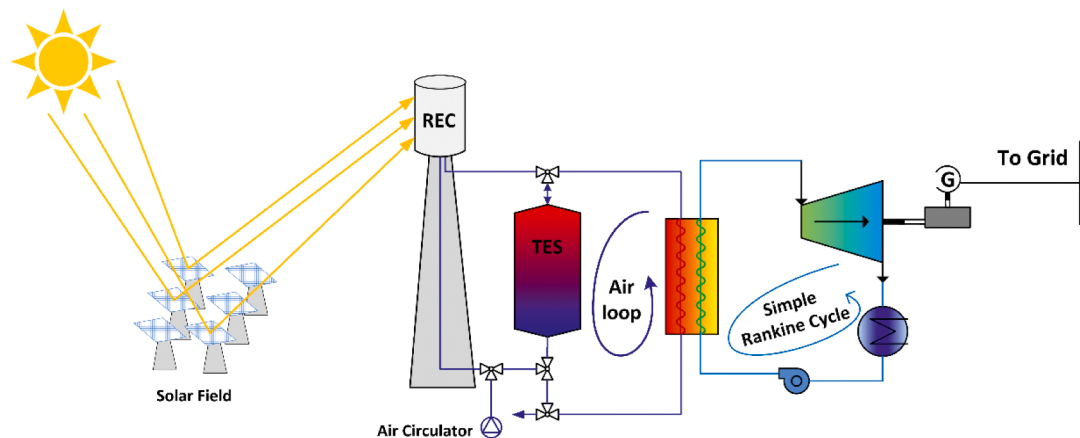


Fig. 1. Schematic layout of a CSP plant including a packed bed TES cycle. Simple Rankine cycle is shown as an example of a power unit.

model [23], has been formulated. The one dimensional, two phases, transient model considers conduction, convection, and radiation heat transfer mechanisms. The main assumptions included in the model can be summarized as:

- Mono-dimensional axial Newtonian plug flow
- Uniformly distributed packed bed of spheres (with a uniform void fraction)
- Negligible temperature gradient in the radial direction
- Heat transfer by radiation accounted by means of a modified effective thermal conductivity in both fluid and solid phase
- Neither mass transfer nor internal heat generation
- Negligible tank's wall heat capacity

The Schumann's model has been improved introducing some additional features. The air, considered HTF, thermodynamic properties have been retrieved by the REFPROP database [24]. The density and specific heat of the solid filler have been evaluated as the mean values of igneous acid rocks related data collected from [25–27], while the rock temperature dependent conductivity has been retrieved from [28]. The thermodynamic properties of the solid filler are reported in Table 1. A layered insulation, comprehensive of a high-temperature Microtherm® insulation layer, a low-temperature Foamglas® insulation layer and a structural shell in steel AISI 316L, has been included in the model. Fig. 2 shows a schematic representation of the considered TES geometry. Consecutive operation cycles (charge-discharge-idle) have been simulated. Each cycle starts with a charge phase followed by a discharge phase. The discharge phase ends when the outlet flow temperature drops below a defined cut off temperature, $T_{cut-off}$, and then an idle period starts. A complete cycle (charge-discharge-idle) has been considered of 24 hours. The charge phase lasts for 8 hours, the discharge duration depends on $T_{cut-off}$, and the idle covers the remaining part of the 24 hours cycle. The one dimensional, two phases, transient model can be summarized by a fluid, Eq. (1), and a solid equation, Eq. (2).

$$\frac{\partial T_F}{\partial t} + \frac{G}{\rho_F \epsilon} \frac{\partial T_F}{\partial x} = \frac{k_{eff}}{\rho_F c_{pf} \epsilon} \frac{\partial^2 T_F}{\partial x^2} + \frac{ha_s}{\rho_F c_{pf} \epsilon} (T_S - T_F) + \frac{U_w D \pi}{\rho_F c_{pf} A \epsilon} (T_\infty - T_F) \quad (1)$$

$$\frac{\partial T_S}{\partial t} = \frac{k_{eff}}{\rho_S c_{ps} (1 - \epsilon)} \frac{\partial^2 T_S}{\partial x^2} + \frac{ha_s}{\rho_S c_{ps} (1 - \epsilon)} (T_F - T_S) \quad (2)$$

where, T is the temperature, ρ is the density, c_p is the specific heat, k_{eff} is the effective thermal conductivity, and the subscripts F and S stand for fluid and solid. G is the HTF mass flow rate per unit cross-section area, a_s is the packed bed surface to volume ratio, U_w is the heat transfer coefficient between the wall and the ambient air, ϵ is the packed bed void fraction, h is the convective heat transfer coefficient between the HTF and the filler material, and D and A are the TES diameter and cross-sectional area. Fig. 2 shows the considered boundary conditions at top and bottom nodes for the fluid equation during the different operation phases, null temperature gradient has been assumed for the solid equation for all boundary conditions. The filling material is considered to be perfectly spherical. The bed void fraction, ϵ , has been assumed

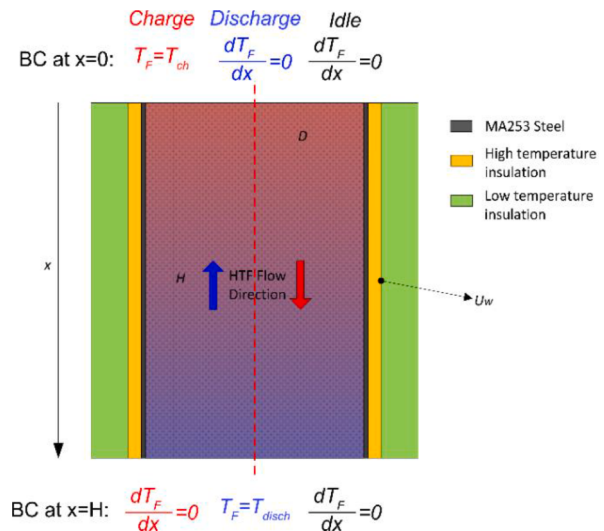


Fig. 2. Schematic representation of the TES layout, including considered boundary conditions for the fluid temperature during charge, discharge and idle periods.

equal to 0.4 and uniform in the whole packed bed, this is a conservative value for hexagonal packing of spheres [29]. The variation in porosity along the inner wall and relative wall channeling effect have been neglected, as justified by a ratio D/d_p higher than 40 [30]. The thermal losses towards the external ambient comprehend convection at the internal surface, between the HTF and the TES tank, conduction through the steel and insulation layers, and convection on the external TES tank surface, leading to an overall heat transfer coefficient U_w , defined as Eq. (3).

$$\frac{1}{U_w} = \frac{1}{a_{in}} + \frac{D}{2} \sum_{j=1}^{n_{ins}} \frac{1}{k_j} \ln \frac{d_{j+1}}{d_j} + \frac{1}{a_{out}} \frac{d_{out}}{d_{ins}} \quad (3)$$

where, a_{in} and a_{out} are the convective heat transfer coefficients on the inside and outside of the TES tank have been evaluated as from [31] and [32], respectively; k_j is the thermal conductivity of the different insulation and steel layers, which have diameters equal to d_j .

The convective heat transfer coefficient between the HTF and the filler material, h^* , has been evaluated by means of the correlation proposed by Coutier and Faber [33], Eq. (4). Differently from other correlations based on spherical particles assumption, the Coutier and Faber correlation was obtained through different experimental setups. Many minor phenomena are already considered in the correlation, avoiding further modelling steps.

$$h^* = \frac{700}{6(1-\epsilon)} G^{0.76} d_p^{0.24} \quad (4)$$

To account for the thermal gradient in the single pebbles the effective heat transfer coefficient h^* has been modified including a term to account for the conduction resistance of the solid pebbles, as proposed in [34] and verified in [35]. The resulting effective heat transfer coefficient h is defined in Eq. (5).

$$\frac{1}{h} = \frac{1}{h^*} + \frac{d_p}{10 \cdot k_s} \quad (5)$$

An effective, temperature dependent, overall thermal conductivity of the packed bed, k_{eff} , has been calculated by means of the model proposed by Kunii and Smith [36], where conduction and radiation within the packed bed and among the single pebbles are considered. The effective thermal conductivity has been evaluated as in Eq. (6).

Table 1

Thermodynamic properties of the solid filler material, as average of data for igneous acid rocks from [23–25], thermal conductivity retrieved from [26].

Property	Symbol	Value	Unit
Density	ρ_s	2850	[kg/m ³]
Specific heat	c_{ps}	1172.5	[J/(kgK)]
Thermal conductivity	k_s	(807 / (350 + (T - 273.15))) + 0.64	[W/(mK)]
Thermal emissivity	ξ_R	0.85	[-]
Particle average diameter	d_p	0.035	[m]

$$\frac{k_{eff}}{k_F} = \varepsilon \left[k_F + \beta \frac{h_{RV} \cdot d_p}{k_F} \right] + \frac{\beta(1-\varepsilon)}{\frac{1}{\phi + \frac{d_p}{k_F} \cdot h_{RS}}} + \gamma \frac{k_F}{k_s} \quad (6)$$

where, β , equal to 0.895, is the ratio between the effective length between centers of adjacent particles in the flow direction and the particle diameter, γ , equal to 2/3, is the ratio between the effective thickness of a solid particle and its diameter; h_{RV} and h_{RS} are the heat transfer coefficients for the thermal radiation from void to void and between solid surfaces, defined as in Eqs. (7) and (8).

$$h_{RV} = \left[4\sigma T^3 + \frac{\varepsilon}{2(1-\varepsilon)} \frac{(1-\xi_R)}{\xi_R} \right] \quad (7)$$

$$h_{RS} = 4\sigma T^3 \left(\frac{\xi_R}{2 - \xi_R} \right) \quad (8)$$

where, ξ_R is the thermal emissivity of the particle surface, and σ is the Stephan-Boltzmann constant, $\sigma = 5.67 \times 10^{-8} \text{ W}/(\text{m}^2 \cdot \text{K}^4)$. The quantity ϕ is a measure of the effective thickness of the fluid film adjacent to the contact surface of two sold particles and it is evaluated with the procedure explained in [36] and summarized by Eqs. (9) and (10).

$$\phi = \phi_2 + (\phi_1 - \phi_2) \frac{\varepsilon - \varepsilon_2}{\varepsilon_1 - \varepsilon_2} \quad (9)$$

$$\phi_i = \frac{1}{2} \frac{\left(\frac{K-1}{K}\right)^2 \sin^2 \theta_{O,i}}{\ln[K - (K-1)\cos\theta_{O,i}] - \frac{K-1}{K}(1 - \cos\theta_{O,i})} - \frac{2}{3} \frac{1}{K} \quad (10)$$

The quantities ϕ_1 and ϕ_2 , in Eq. (9) correspond to the ϕ values for the loose and close packing arrangements, respectively, are evaluated as in Eq. (10). The void fractions for the two extreme arrangements are equal to $\varepsilon_1 = 0.476$ and $\varepsilon_2 = 0.26$, K is the ratio between the solid and fluid thermal conductivity ($K = k_s/k_F$), and $\sin^2 \theta_{O,i} = 1/n_i$, where n_i corresponds to the number of contact points on a semispherical surface for each particle, equal to 1.5 in the loose packing arrangement and to $3\sqrt{4}$ in the close packing arrangement. The method explained by Cheng and Hsu [37] has been applied to share the effective conductivity contributions between the fluid and the solid phase, obtaining $k_{F,eff}$ and $k_{S,eff}$, respectively. Particularly, the contribution to the effective thermal conductivity of only thermal conduction through fluid and solid phases has been accounted by $k_{0,eff}$, Eq. (11), [37].

$$\frac{k_{0,eff}}{k_F} = \varepsilon + \frac{\beta(1-\varepsilon)}{[\phi + \gamma/K]} \quad (11)$$

Then, the effect on the effective thermal conductivity due only to thermal radiation has been evaluated as $k_{R,eff} = k_{eff} - k_{0,eff}$. Finally, the effective thermal conductivity has been subdivided into the two phases, $k_{F,eff}$ and $k_{S,eff}$, as in Eq. (12).

$$\begin{cases} k_{F,eff} = (\varepsilon k_F + f k_F) \\ k_{S,eff} = ((1-\varepsilon)k_S - f k_S) + k_{R,eff} \end{cases} \quad (12)$$

where the coefficient f , defined in Eq. (13), accounts for the tortuosity of the bed.

$$f = \frac{k_{0,eff} - \varepsilon k_F - (1-\varepsilon)k_S}{k_F - k_S} \quad (13)$$

The pressure drop along the packed bed has been evaluated by the Ergun's correlation, Eq. (14), [38].

$$\frac{\Delta p}{H} = 1.75 \left(\frac{1-\varepsilon}{\varepsilon^3} \right) \frac{G^2}{\rho_F d_p} + 150 \left(\frac{(1-\varepsilon)^2}{\varepsilon^3} \right) \frac{G \mu_F}{\rho_F d_p^2} \quad (14)$$

The implemented model has been validated by comparing the temperature profiles across the storage calculated in the present study with the experimental and modelling data published in [5,30]. The reference

studies analyzed the thermal behavior of a packed bed TES working with air as HTF and steatite, a magnesium silicate rock. The values of the considered design parameters during the validation process are summarized in Table 2, [5]. The comparison of the fluid temperature profiles along the TES height is illustrated in Fig. 3, where continuous lines are the results of the present model, different markers show the experimental data [34], and dotted lines represent the modelling results exposed in [5]. The present model calculates the fluid temperature with an average error lower than 6°C with respect to the experimental data. A maximum error of about +50°C is recorded for the top measurement point after 1200 seconds. This larger error is explained by the fact that during the experiment presented in [5] some delays in reaching the set inlet fluid temperature (550°C) were observed. These delays are not accounted by the present model, which considers a constant fluid inlet temperature during the whole charge phase. In general, good agreement with the reference data is achieved and the model can be used for further studies.

2.2. Transient boundary conditions

To the authors' knowledge, in most of the state of the art optimization studies about packed bed TES, constant working conditions have been assumed. Particularly, a constant HTF mass flow rate during charge and discharge has been modeled. Nevertheless, due to the inherent variability of the solar energy, the real working conditions of a TES integrated in a CSP plant are variable and the HTF mass flow rate will mainly depend on the actual DNI level. CSP plants are usually operated at a constant electricity output from the power unit, storing the excess of thermal energy during the day until the state of charge of the TES reaches its maximum value. During the night, the TES is discharged in order to keep a constant power production until the state of charge of the TES drops below its minimum allowed value. In the present work, two different HTF mass flow rate profiles have been simulated to assess the influence of quasi-dynamic HTF mass flow rate on the thermal behavior of a large scale packed bed TES:

A constant HTF mass flow rate, equal to \dot{m}_{chDES} as in Eq. (15), considered throughout the whole charging period.

$$\dot{m}_{chDES} = \frac{E_{TES}}{c_{p,\text{avg}} (T_{ch} - T_{disch}) \cdot t_{ch}} \quad (15)$$

where, E_{TES} is the design energy capacity of the TES, T_{ch} and T_{disch} are the fluid inlet temperatures during charge and discharge, $c_{p,\text{avg}}$ is the specific heat at an average temperature between T_{ch} and T_{disch} , and t_{ch} is the design charge phase duration.

A variable $\dot{m}_{chSEASONS}$ profile evaluated for four characteristic days (21st March, 21st June, 23rd September, 22nd December), as in Eq. (16).

$$\dot{m}_{chSEASONS}(t) = \dot{m}_{chDES} \frac{DNI(t) \cdot \eta_{SF}(t)}{DNI \cdot \bar{\eta}_{SF}} \quad (16)$$

Table 2

Values of the main parameters used for the validation of the packed bed TES model, as from [5].

Parameter	Symbol	Value	Unit
TES inlet temperature	T_{in}	550	[°C]
Ambient temperature	T_∞	20	[°C]
Specific HTF mass flow rate	G	0.225	[kg/(m ² ·s)]
Packed bed height	H	1.2	[m]
Packed bed diameter	D	0.148	[m]
Void fraction	ε	0.4	[·]
Particle average diameter	d_p	0.02	[m]
Solid density	ρ_s	2680	[kg/m ³]
Solid specific heat	c_{ps}	1068	[J/(kg·K)]
Solid thermal conductivity	k_s	2.5	[W/(m·K)]
External heat transfer coefficient	U_w	0.678	[W/(m ² ·K)]

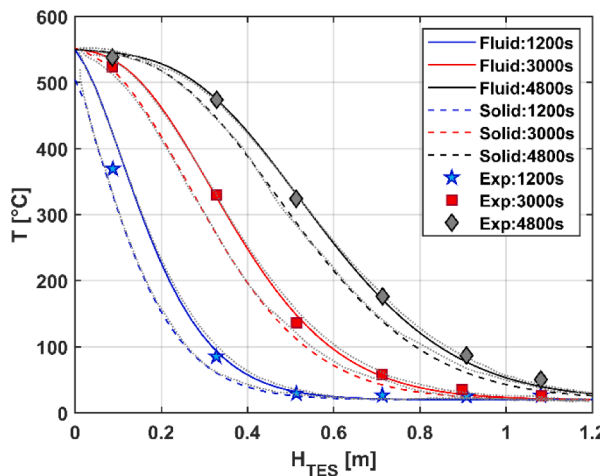


Fig. 3. Validation of the packed bed TES model against experimental and modelling data published in [5,30].

where, $DNI(t)$ and $\eta_{SF}(t)$ are the time dependent values of DNI and the solar field efficiency, and \overline{DNI} and $\overline{\eta_{SF}}$ are the average values of DNI and solar field efficiency. Casablanca, Morocco ($33.60^{\circ}\text{N}, 7.62^{\circ}\text{W}$, GHI = 1857 kWh/m^2) is the selected location. The solar field optical efficiency has been calculated via the commercial software System Advisor Model [39] considering the design parameters summarized in Table 4.

The resulting seasonal HTF mass flow rate reflects the influence of the variability of both the DNI and solar field optical efficiency. The DNI and solar field optical efficiency profiles are represented in Fig. 4(a), while the different HTF mass flow rate profiles are shown in Fig. 4(b). Fig. 4(b) shows the full HTF mass flow rate profiles including the discharge and idle operations (at constant negative and null HTF mass flow rate), which occur when $DNI(t) = 0$ as explained in Section 2.1.

2.3. Economic model

A simple economic model has been developed to evaluate CAPEX and LCoS for the studied packed bed TES. The CAPEX has been calculated as the sum of all materials costs, as in Eq. (17).

$$\text{CAPEX} = \sum_{i=1}^{N_{\text{mat}}} c_i V_i \quad (17)$$

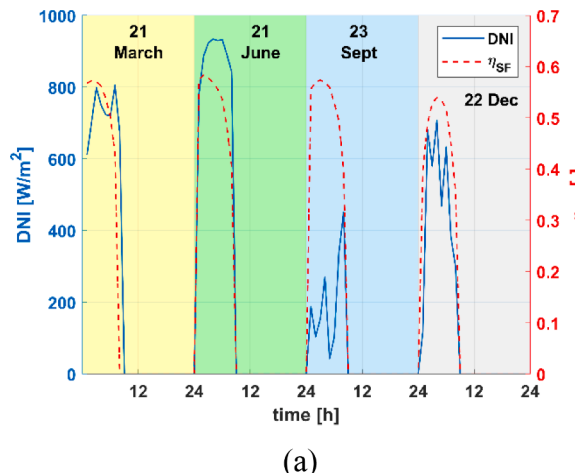


Fig. 4. (a) DNI and solar field optical efficiency, η_{SF} , during the selected four representative seasonal days (21st March, 21st June, 23rd September and 22nd December); (b) HTF mass flow rate for the design case and for the seasonal case, identified by four representative seasonal days (21st March, 21st June, 23rd September and 22nd December).

where N_{mat} is the number of TES materials, c_i are the specific costs of materials as reported in Table 3 (as collected from [15] and specific quotations), and V_i is the volume of each material. The OPEX, defined in Eq. (18), is the operational cost evaluated as the sum of the operation and maintenance costs, assumed equal to 2 % of the CAPEX, and the electricity costs for circulating the HTF through the TES units during both charge and discharge. The energy for air circulation has been evaluated as the sum of the energy spent to overcome the pressure drop induced by the packed bed (Δp_{ch} and Δp_{disch}) and circulate the HTF through the TES during both charge and discharge operation, as from Eq. (19).

$$\text{OPEX} = 0.02 \cdot \text{CAPEX} + E_{\text{pump}} c_{el} N_{\text{TES}} \left(\frac{365}{4} \right) \quad (18)$$

$$\begin{aligned} E_{\text{pump}} &= E_{\text{pump}_{ch}} + E_{\text{pump}_{disch}} \\ &= \left[\int_0^{t_{ch}} \frac{AN_{\text{TES}} G_{ch}(t) \Delta p_{ch}(t)}{\rho_F} dt + \int_0^{t_{disch}} \frac{AN_{\text{TES}} G_{disch}(t) \Delta p_{disch}(t)}{\rho_F} dt \right] \frac{1}{\eta_{compr}} \end{aligned} \quad (19)$$

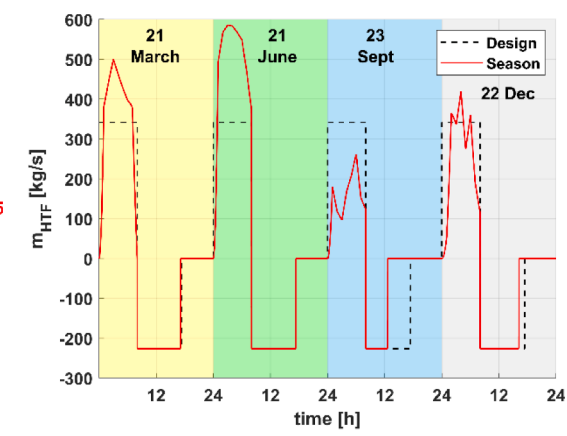
In Eq. (18) c_{el} is a fixed electricity price, assumed equal to $0.11 \text{ \$/kWh}_{\text{el}}$, N_{TES} is the number of parallel storage units. In Eq. (19) A is the TES cross-sectional area, ρ_F is the fluid density, G_{ch} and G_{disch} are the HTF mass flow rates per unit cross-section area during charge and discharge, Δp_{ch} and Δp_{disch} , are the pressure drops induced by the TES unit during charge and discharge, and η_{circ} is the air circulator efficiency, assumed equal to 0.95.

The LCoS has been evaluated as in Eq. (20). With respect to the Lazard's definition [17] the charging cost, related to the production of the thermal energy needed to charge the TES, have been neglected. This cost depends on the charging technology used and, for the sake of this work, is considered constant and independent on the TES design choices. This choice has been adopted to limit the scope of this study to the TES

Table 3

Specific costs of TES main components, as collected from [13] and specific quotations.

Component	Value	Unit
Rocks	66	$[\$/\text{m}^3]$
High-temperature insulation	4269	$[\$/\text{m}^3]$
Low-temperature insulation	616	$[\$/\text{m}^3]$
MA253 Steel	42354	$[\$/\text{m}^3]$
Foundation	1210	$[\$/\text{m}^2]$



unit. Additional consideration regarding the adopted discounting are explained by Kost [40].

$$LCoS = \frac{CAPEX + \sum_{n=1}^{N_{op}} \frac{OPEX}{(1+r)^n}}{\sum_{n=1}^{N_{op}} \frac{E_{NET}}{(1+r)^n}} \quad (20)$$

In Eq. (13), N_{op} is the TES operational life, equal to 30 years, and r is discount rate, equal to 7 %, as from [40], and E_{NET} is the net electricity output recoverable from the TES unit. As the TES itself stores and provides thermal energy, in order to evaluate the net electrical production a conversion efficiency of a typical Rankine cycle, η_{cycle} , has been applied (Rankine power cycles are the state of the art technology for CSP). The conversion efficiency is assumed to be linearly proportional to the TES outflow temperature during discharge. A maximum value of $\eta_{cycle,max} = 0.42$ and a minimum of $\eta_{cycle,min} = 0.30$ have been assumed at the maximum TES outflow temperature (T_{ch} equal to 700°C) and at minimum TES outflow temperature equal to $T_{cut-off}$. The resulting conversion efficiency can be written as Eq (21). Fig. 5 shows the conversion efficiency during a discharge process of the TES unit.

$$\eta_{cycle}(t) = \eta_{cycle,max} - (\eta_{cycle,max} - \eta_{cycle,min}) \cdot \left(1 - \frac{T_{outTES}(t) - T_{cut-off}}{T_{ch} - T_{cut-off}} \right) \quad (21)$$

3. Design methodology

In the present work, a methodology for the design of a packed bed TES is proposed. Fig. 6 shows the flowchart of the methodology. As a first step, an initial design based on a set of steady requirements is performed. The TES volume is evaluated accordingly to Eq. (22)

$$V_{TES} = \frac{E_{TES}}{(\rho c_p)_{eff} \Delta T_{DES} N_{TES} \eta_0} \quad (22)$$

where, E_{TES} is the TES energy capacity, calculated by multiplying the number of TES discharge hours at the design thermal power, $(\rho c_p)_{eff}$ is the effective heat capacity of the TES evaluated at the average temperature (between maximum, T_{ch} , and minimum, T_{disch}), ΔT_{DES} is the design maximum temperature difference in the TES, N_{TES} is the number of TES units, and η_0 is the preliminary efficiency, assumed equal to 0.85. The TES preliminary efficiency oversizes the storage unit to account for the thermal losses and a decrease in the outlet temperature during the second phase of the discharge. Such concept has been previously introduced in [16] as storage mass β , equivalent to $1/\eta_0$. The assumed value of η_0 has been based on the authors' experience and it is about the mean value among different studies presented in literature [5,6]. The working temperatures depend on the coupled power unit. In the present work, the use of a steam cycle has been assumed and a maximum and a

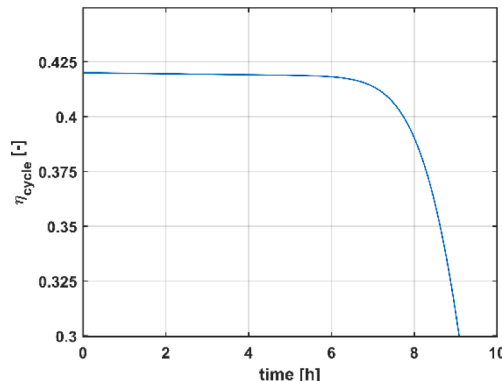


Fig. 5. Considered power cycle conversion efficiency (thermal to electrical power) during the discharge process of the TES unit.

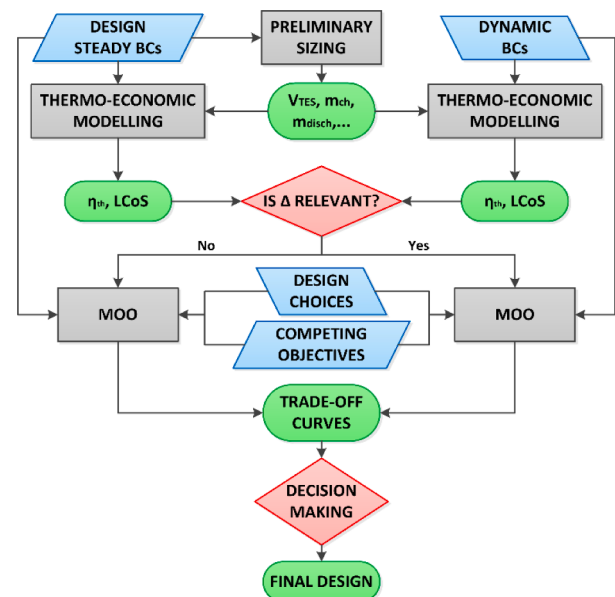


Fig. 6. Flowchart describing the proposed TES design methodology, as well as the methodology followed during this work.

minimum TES working temperature of 700°C and 120°C have been considered. As part of the preliminary sizing, the design HTF mass flow rate during charge and discharge have been evaluated as the amount of HTF able to deliver the required thermal energy under design working conditions, Eqs. (23) and (24),

$$\dot{m}_{ch} = \frac{E_{TES}}{\Delta h|_{T_{min}}^{T_{max}} t_{ch,DES} N_{TES} \eta_0} \quad (23)$$

$$\dot{m}_{disch} = \frac{E_{TES}}{\Delta h|_{T_{min}}^{T_{max}} t_{disch,DES} N_{TES} \eta_0} \quad (24)$$

where, $\Delta h|_{T_{min}}^{T_{max}}$ is the maximum fluid enthalpy change, $t_{ch,DES}$ and $t_{disch,DES}$ are the required design charge and discharge phase duration, respectively. At this preliminary stage, the number of TES units have been considered as a fixed value, assuming a maximum value of the TES height of 15 m.

Second step of the proposed design methodology is to evaluate the TES thermodynamic behavior for a number of consecutive cycles, to ensure that a steady state cyclic behavior is reached four consecutive cycles are considered in this work. At this stage, steady state boundary conditions (HTF mass flow rate and T_{ch}) should be considered. An iterative procedure adjusting the preliminary efficiency can be performed in order to obtain a base scenario able to fulfill the main TES discharge requirements (TES outlet temperature higher than $T_{cut-off}$ at the end of the discharge period). The TES economic performance should be also evaluated.

As a third move, the thermo-economic performance of the TES should be evaluated including realistic dynamic boundary conditions. In normal working conditions, \dot{m}_{ch} depends on the upstream energy input. At this point, the thermo-economic KPIs obtained during the TES modelling under steady and dynamic boundary conditions should be compared. If a relevant difference between them is detected, the dynamic boundary conditions should be considered during the following optimization steps.

As a last step, the relevant design variables (geometrical and operational parameters) and competing objectives should be identified. Then, a full multi-objective optimization should be performed to fully explore the range of variability of the identified design parameters, and to evaluate the different possible optimal TES designs in the thermo-

economic perspective. As a result of this MOO different trade-off curves can be identified. It is important to note that all TES designs belonging to such Pareto curves are equally optimal from a mathematical point of view. The final design choice would depend on the involved entities, as an example: constructor companies would be mostly interested by TES designs with a minimal CAPEX, contrarily operator companies would be attracted by design enabling the lowest LCoS. In the following paragraphs, additional details about the TES preliminary design and its multi-objective optimization are presented. The results of applying the proposed methodology to a specific case study are shown in Section 4. In paragraph 4.1 the thermo-economic performance of the TES unit are presented under steady and dynamic boundary conditions. In Section 4.2 the results of different MOOs under steady and dynamic boundary conditions are discussed and the influence of the considered design parameters is investigated.

3.1. Preliminary design under steady and dynamic boundary conditions

As base design case, the main TES design parameters reported in Table 4 are considered. The thermo-economic performance of the TES are evaluated based on:

- TES overall efficiency, $\eta_{th,ovr}$, defined as the ratio between the energy outflow, Eq. (25), and the sum of inlet energy, Eq. (26), and energy spent to overcome the HTF pressure drop during both charge and discharge phase, Eq. (27). The air circulation energy during operation have been evaluated starting from Eq. (19), without considering the compressor efficiency, since $\eta_{th,ovr}$ is relative only to thermal quantities.
- Duration of the discharge period, t_{disch} , (with TES outlet temperature higher than $T_{cut-off}$).
- Thermal energy outflow, $E_{TES,out}$, defined as in Eq. (25).
- Thermocline thickness during discharge periods, TC_{disch} , defined as the percentage of TES occupied by the thermocline region, Eq. (28).
- Capital expenditure, CAPEX, as defined in Eq. (17).
- Levelized Cost of Storage, LCoS, as defined in Eq. (20).

$$E_{TES,out} = \int_0^{t_{disch}} AN_{TES} G_{disch}(t) c_{p_F}(t) [T_{F,out}(t) - T_{F,in}] dt \quad (25)$$

$$E_{TES,in} = \int_0^{t_{ch}} AN_{TES} G_{ch}(t) c_{p_F}(t) [T_{F,in} - T_{F,out}(t)] dt \quad (26)$$

$$\eta_{th,ovr} = \frac{E_{TES,out}}{E_{TES,in} + E_{pump,ch} + E_{pump,disch}} \quad (27)$$

$$TC_{disch} = \frac{|x|_{T_F=T_{ch}-50^\circ C} - |x|_{T_F=T_{disch}+50^\circ C}}{H} \quad (28)$$

Table 4

Main TES design parameters defined as traditional values for packed bed TES or as from industrial requirements.

Parameter	Symbol	Value	Unit
Design direct normal irradiance	DNI _{DES}	800	[W/m ²]
TES energy capacity	E _{TES}	4'080	[MWh _{th}]
TES thermal power	P _{TES}	340	[MW _{th}]
Charge duration	t _{ch,DES}	8	[h]
Design discharge duration	t _{disch,DES}	12	[h]
Fluid top inlet temperature during charge	T _{ch}	700	[°C]
Fluid bottom inlet temperature during discharge	T _{disch}	120	[°C]
CSP plant solar multiple	SM	2.5	[·]
Cut-off temperature during discharge	T _{cut-off}	640	[°C]
Number of TES units	N _{TES}	3	[·]
Aspect ratio ($\alpha = H/D$)	α	0.75	[·]
Particles average diameter	d _p	0.035	[m]
Preliminary efficiency	η_0	0.85	[·]

The TES techno-economic performance is investigated considering steady and quasi-dynamic boundary conditions (namely a variable \dot{m}_{ch} , defined as design and seasonal case, respectively, in Section 2.2).

3.2. Multi-objective optimization

Sensitivity analyses and optimization works presented in the literature indicate the presence of trade-offs between costs and efficiency of the packed bed TES. In the present work, different multi-objective optimizations are performed and compared. In doing so, the reliability of using the CAPEX as the main economic indicator to optimize the packed bed TES is assessed, and the influence of unsteady boundary conditions is investigated. As a result, different optimum trade-off curves and optimal TES designs are identified. To assess the techno-economic performance of the packed bed TES, the following KPIs are considered: overall thermal efficiency, $\eta_{th,ovr}$ (Eq. (27)), LCoS (Eq. (20)), and CAPEX (Eq. (17)). Unitary weights have been considered for all objectives in the three MOOs. The design energy capacity, E_{TES} , has been kept constant throughout the optimization, therefore the capital cost can be compared in absolute terms. Several decision variables have been investigated: TES aspect ratio, α , preliminary efficiency, η_0 , number of TES units, N_{TES} , particle diameter, d_p and HTF mass flow rate during discharge, \dot{m}_{disch} . These variables have been selected since they are expected to have relevant influences on thermal performance, pressure losses and economic indicators. The multi-objective optimization problems are theoretically defined, including objective functions and constraints, as in Table 5, and they have been repeated for both HTF mass flow rate profiles depicted in Fig. 4(b). The boundaries for aspect ratio and TES preliminary efficiency have been selected based on literature data [8]. The possible range for the number of TES units depends on structural limitations for the tank constructions. Operational considerations explain the selection of the constraints for d_p and \dot{m}_{disch} . Too small particle diameter would imply excessive pressure drops, while too large ones would limit the TES thermal performance by introducing large pebble internal temperature gradients. The selected range of HTF mass flow rate during discharge permit to maintain t_{disch} close to its design value. The multi-objective optimizations are performed by means of the evolutionary genetic algorithm implemented in a MatLab 2019 environment [41–43]. The evolutionary genetic algorithm is a stochastic search optimization method, which enables to globally solve optimization problems where continuity and differentiability of the fitness function is not guaranteed [44].

4. Results and discussion

4.1. Preliminary design under steady and quasi-dynamic boundary conditions

The thermodynamic behavior of the TES under both steady and quasi-dynamic boundary conditions is represented in Fig. 7 by means of the fluid temperature at the top and mid height (solid and dashed lines, respectively, in Fig. 7(a)) and the SOC (Fig. 7(b)) during charge. The

Table 5
Multi-objective optimizations theoretical definitions.

	MOO. A	MOO. B	MOO. C
Objective Function:	$\min([-\eta_{th,ovr}; CAPEX])$	$\min([LCoS; CAPEX])$	$\min([-\eta_{th,ovr}; LCoS])$
$\bar{F}(\alpha, N_{TES}, d_p, \dot{m}_{disch}, \eta_0)$			
Constraints		$0.75 < \alpha < 1.25; 3 < N_{TES} < 6; 0.02 < d_p < 0.1 \text{ m}; 500 < \dot{m}_{disch} < 800 \text{ kg/s}; 0.4 < \eta_0 < 1$	

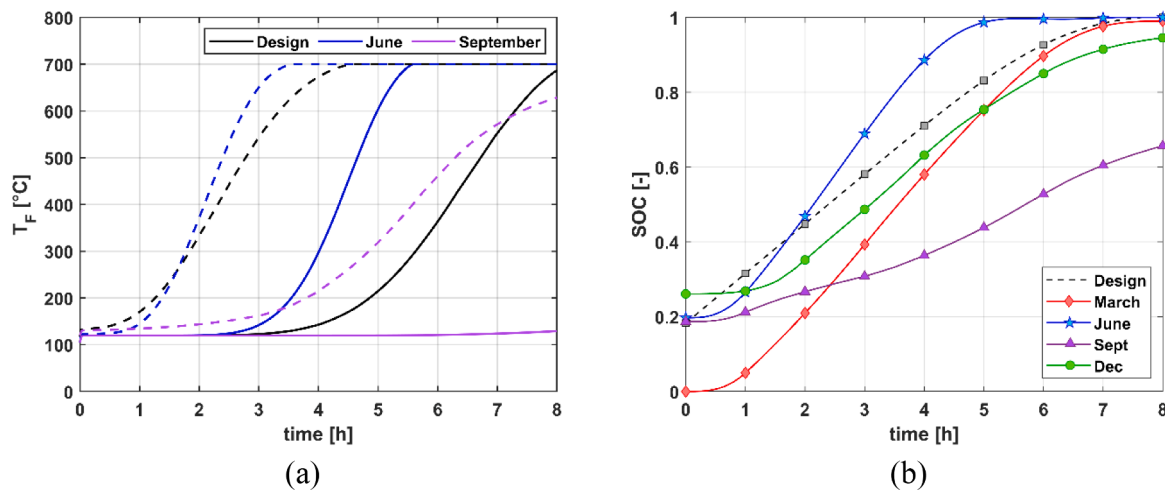


Fig. 7. (a) Fluid temperature during charge at the top ($x = H$, solid lines) and medium height of the TES ($x = H/2$, dashed lines), for design case and two representative days (June and September); (b) TES SoC during charge for design case and four representative day.

design case shows a complete TES charge after 8 hours. The June case shows a faster charge, driven by higher \dot{m}_{HTF} , with a unitary SoC already after about 5.5 hours. Thinner thermocline and faster temperature growth along the TES axis can be also identified for the June case. Contrarily, the September case shows a slower charging process, driven by lower \dot{m}_{HTF} . The fluid temperature during charge at the mid height of the TES increases at a slower rate and the TES outlet temperature remains almost constant and equal to T_{disch} , which implies no thermocline discharge. The variable \dot{m}_{HTF} profile during the September case (with two peaks after about 1 and 6 hours of the charge phase) is mirrored by the SoC profile, which shows higher growth slopes at the \dot{m}_{HTF} peaks.

The main results for the preliminary TES design under both steady and quasi-dynamic boundary conditions are also reported in Table 6. The TES performance for the seasonal case are reported for each considered characteristic day (21st March, 21st June, 23rd September, 22nd December). The TES techno-economic performance is widely affected by variable \dot{m}_{HTF} during charge. The TES overall thermal efficiency, $\eta_{th,ovr}$, is largely affected by variable HTF mass flow rate; values within the range +2 % to -21 % with respect to the design case are recorded in the seasonal scenario. Higher \dot{m}_{HTF} means faster HTF flow through the TES, and a higher HTF speed leads to improved convective heat transfer coefficient between the TES solid filler and the HTF. Thus, reduced heat transfer losses and thinner thermocline region can be achieved. Looking at the thermocline thickness, lower \dot{m}_{HTF} implies little or no thermocline discharge during charge (the thermocline region does not reach the bottom part of the TES unit). Without thermocline discharge, its thickness grows during the following discharge phase, leading to further thermocline degradation (as from September case). Variable HTF mass flow rates are also reflected by non-constant speeds in the thermocline thickness growth during charge. Longer useful discharge period are recorded for the days with a higher \dot{m}_{HTF} during charge. This is influenced by two major factors: firstly, when operating the TES with higher \dot{m}_{HTF} during charge more energy can be stored in the unit; secondly, thinner thermocline regions develop and the TES outflow

temperature remains longer above the cut-off limit. The variable boundary conditions affect only the operation of the TES unit, not its design, thus the CAPEX is not modified. The seasonal case leads to an increase of the LCoS of about 55 % with respect to the design case. Reasons for that can be found in the large variability between consecutive cycles, which does not enable for the TES working conditions stabilization, and causes worse energy outputs. Furthermore, the HTF circulation energy consumption increases with the third power of the specific mass flow rate, so higher E_{pump} are recorded. In conclusion, wide differences, between the design and seasonal scenarios, can be recorded for both $\eta_{th,ovr}$ and LCoS. Such results suggest that during TES design and optimization, realistic variable boundary conditions should be taken into consideration and properly evaluated.

4.2. Multi-objective optimization: case A

Fig. 8 shows the results of the multi-objective optimization A. The TES overall thermal efficiency, $\eta_{th,ovr}$, is plotted against the TES CAPEX for steady (Fig. 8 (a)) and quasi-dynamic (Fig. 8(b)) boundary conditions. The two Pareto curves are shown and the LCoS is represented by the color of the dots. Each of the represented dots corresponds to a possible TES design. Some selected TES design points, namely $LCoS_{minD}$, $\$_{minD}$, η_{maxD} , A_D , $LCoS_{minS}$, $\$_{minS}$, η_{maxS} , A_S , and B_S belonging to the Pareto curves identified in the MOOs are also reported. As a reference, the values of both decision variables and objectives for these points are reported in Tables 7 and 8, for both study cases. The results show that the quasi-dynamic HTF profile leads to lower TES thermal efficiency. The maximum $\eta_{th,ovr}$ for the seasonal case can be achieved at a lower CAPEX than the design point (12.33 M\$ for the seasonal case against 12.65 M\$ for the design case). Larger capital investments enable higher TES thermal efficiencies. In the seasonal case, the Pareto curve is steeper, leading to faster $\eta_{th,ovr}$ decrease with decreasing CAPEX. Minimum LCoS TES designs are far from the Pareto Frontier since high CAPEX are required. However, in the design case, moving along the optimal curve

Table 6
Main results for different HTF mass flow rate profiles (Design and Seasonal).

Parameter	Unit	Design	March	June	September	December
$\eta_{th,ovr}$	[-]	0.917	0.724	0.859	0.775	0.934
$E_{TES,out}$	[MWh _{th}]	3926.20	3795.9	3900.8	1902.3	3397.8
t_{disch}	[h]	9.4	9.10	9.35	4.62	8.17
Max TC _{disch}	[%]	35	37.5	35	51.5	43
CAPEX	[M\$]			8.64		
LCoS	[\$/MWh _e]	29.04			45.01	

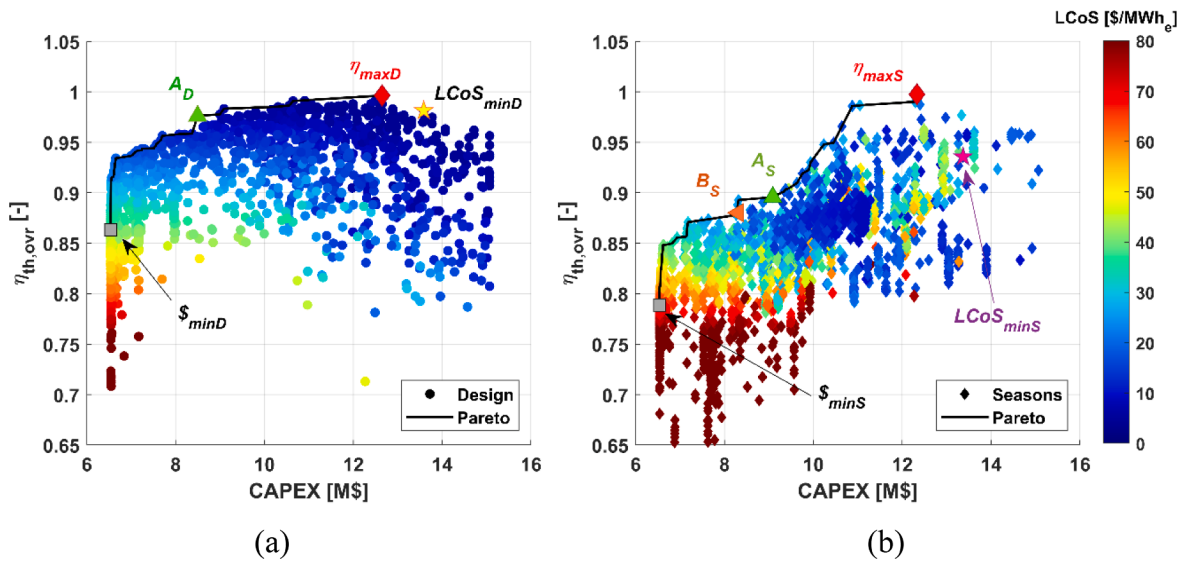


Fig. 8. (a) Multi-Objective Optimization A results, TES thermal efficiency versus CAPEX under steady boundary conditions, with LCoS indicated by the color of dots; (b) Multi-Objective Optimization A results, TES thermal efficiency versus CAPEX under quasi-dynamic boundary conditions, with LCoS indicated by the color of dots.

Table 7

Main thermo-economic results and decision variables values for selected points along Pareto's frontiers under design steady boundary conditions.

		LCoS [\$/MWh _e]	$\eta_{th,ovr}$ [-]	CAPEX [M\$]	OPEX [M\$]	α [-]	N_{TES} [-]	d_p [m]	η_0 [-]	\dot{m}_{disch} [kg/s]
DESIGN	η_{maxD}	4.05	0.99	12.65	1.46	0.75	6	0.1	0.52	600
	S_{minD}	39.87	0.86	6.54	19.39	1.14	3	0.064	1.00	565.7
	$LCoS_{minD}$	3.97	0.98	13.59	1.36	0.75	6	0.1	0.47	598.6
	A_D	7.08	0.97	8.49	3.40	0.75	3	0.1	0.7	515.6

Table 8

Main thermo-economic results and decision variables values for selected points along Pareto's frontiers under seasonal quasi-dynamic boundary conditions.

		LCoS [\$/MWh _e]	$\eta_{th,ovr}$ [-]	CAPEX [M\$]	OPEX [M\$]	α [-]	N_{TES} [-]	d_p [m]	η_0 [-]	\dot{m}_{disch} [kg/s]
SEASONS	η_{maxS}	20.48	0.99	12.33	9.71	0.75	4	0.025	0.45	575.0
	S_{minS}	67.25	0.79	6.54	23.25	0.75	3	0.073	1.00	552.7
	$LCoS_{minS}$	7.51	0.94	13.37	2.28	0.76	6	0.077	0.48	557.8
	A_S	27.68	0.90	9.09	11.95	1.00	3	0.060	0.62	535.1
	B_S	16.95	0.88	8.31	5.22	0.87	5	0.099	0.88	542.2

the LCoS increases for higher TES thermal efficiencies. Looking at the discrete points, some TES design which belong to both the MOO A and MOO B Pareto curves can be identified in the central region of the present Pareto curve. Points A_D , A_S and B_S are reported in Fig. 8, but other designs belonging to the MOO B Pareto can be found along the present optimal trade-off curve particularly in the range with low CAPEX and relatively low $\eta_{th,ovr}$.

The exploited optimization method enables understanding the influence of the decision variables over the predefined objectives. Fig. 9 shows the influence of the particle diameter, number of TES units and preliminary efficiency on both objectives. In the context of MOO A under steady boundary conditions, an increase of d_p is requested to maximize the TES thermal efficiency. Particularly, the minimum and maximum $\eta_{th,ovr}$ are recorded for d_p equal to 0.065 and 0.1 m, respectively (Fig. 9(a)). Contrarily, in the seasonal case, all points along the Pareto frontier register a particle diameter smaller than 0.07 m (Fig. 9(b)). As d_p moves towards smaller values, the available heat transfer area within the packed bed increases, and the thermal performance improves. Particularly, the thermal front becomes steeper and the internal heat losses, due

to poor heat transfer coefficients between the two phases, decrease. Consequently, the discharge period extends. However, pressure losses increases exponentially as d_p decreases (as from Eq. (14)), because the air stream faces a higher resistance. This trade-off is the basis for the choice of optimal particle diameter.

A higher number of TES enables improving the TES thermal efficiency. In the design case, the Pareto front is given by the envelope of the maximum region of the $\eta_{th,ovr}$ versus CAPEX curves for different number of TES units. Contrarily, considering quasi-dynamic \dot{m}_{HTF} , Fig. 9(d), the majority of the optimal configurations have only three or four TES units. In general, more TES units, for the same overall energy capacity, means that the volume of each TES will be smaller, however also the HTF mass flow rate will be reduced since the total one will be divided in more streams. Therefore, the convective heat transfer within the bed will not be largely influenced. Differently, higher N_{TES} causes both a reduction of the pressure losses, particularly relevant at high α , since the TES height is shorter, and an increase of the specific heat losses toward the environment. More TES units for the same overall TES volume require a higher capital expenditure due to a decreased compactness level of the system.

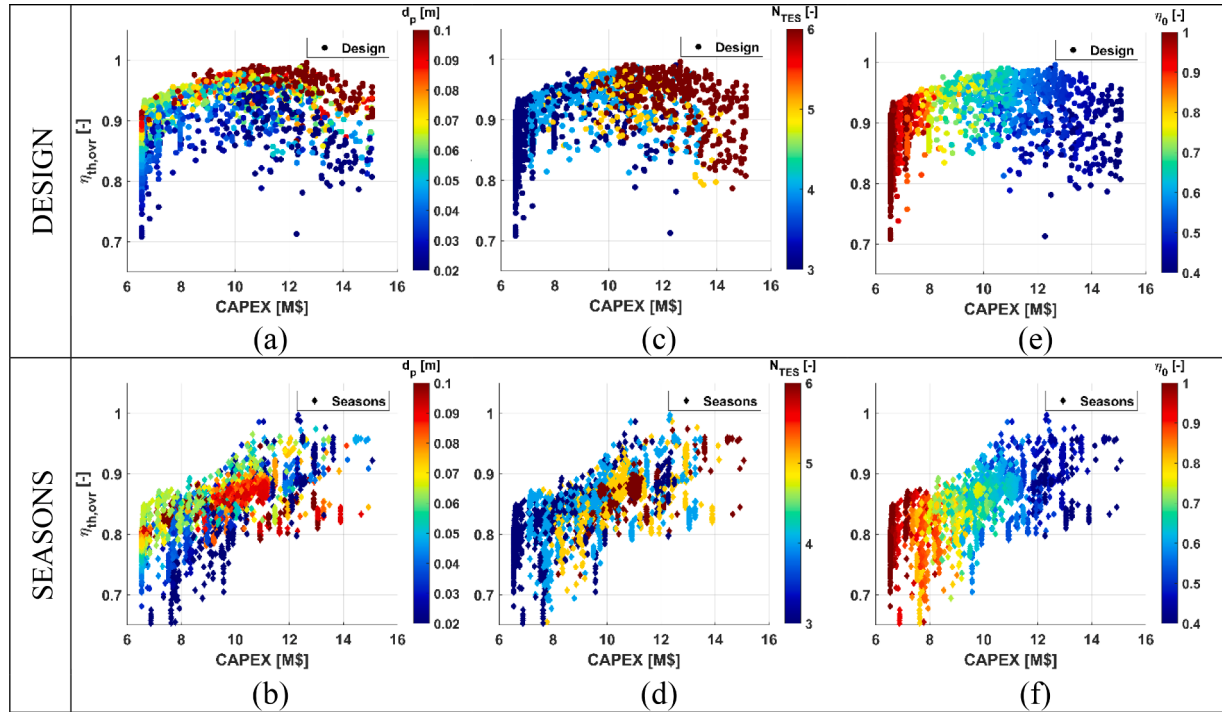


Fig. 9. TES thermal efficiency versus CAPEX for MOO A, with color of dots given by particle diameter for design (a) and seasonal (b) case. TES thermal efficiency versus CAPEX for MOO A, with color of dots given by number of TES units for design (c) and seasonal (d) cases. TES thermal efficiency versus CAPEX for MOO A, with color of dots given by preliminary efficiency for design (e) and seasonal (f) cases.

The influence of both particle diameter and number of TES units is tightly connected with the considered preliminary efficiency, η_0 , whose influence is reported in Figs. 9(e) and (f). An increase in the thermal efficiency is achieved by an overrating of the TES volume; however, this leads also to higher CAPEX. Maximum $\eta_{th,ovr}$ are recorded for η_0 equal to 0.52 and 0.45 in the design and season case, respectively.

In general, under steady boundary conditions, to improve the TES overall thermal efficiency it is necessary to oversize the TES (by reducing η_0) while decreasing the TES aspect ratio and increasing the number of TES units and the particle diameter to limit the pressure losses. Under quasi dynamic HTF mass flow rate boundary conditions, to enhance $\eta_{th,ovr}$, moving along the Pareto frontier, more importance is devoted to

the TES thermal performance. Thus, a decrease in η_0 is required while keeping a relatively small particle diameter and a low number of TES unit; the pressure losses are kept limited by a decreasing aspect ratio. However, in the season case, an interesting TES design region can be identified in the range CAPEX = [9–11] M\$ and $\eta_{th,ovr} = [0.85–0.9]$, where low LCoS are also recorded. In this region, together with intermediate η_0 (between 0.6 and 0.7), large particle diameter and high N_{TES} are also selected. As expected, to minimize the TES CAPEX the lowest number of TES and a unitary initial efficiency are calculated.

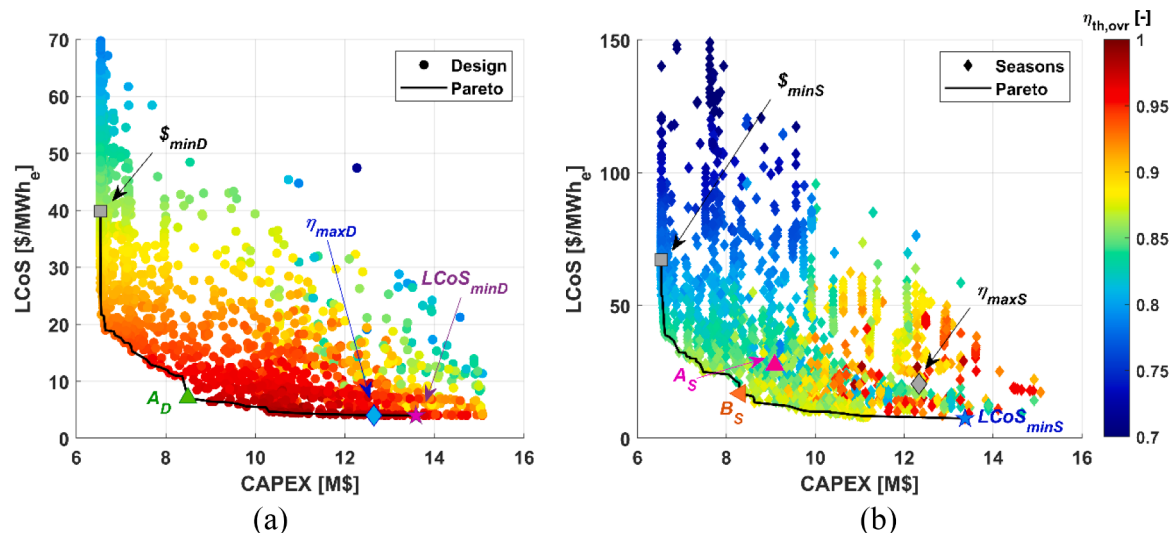


Fig. 10. (a) Multi-objective optimization B, LCoS versus CAPEX under steady boundary conditions, with TES thermal efficiency indicated by the color of dots; (b) Multi-objective optimization B, LCoS versus CAPEX under quasi-dynamic boundary conditions, with TES thermal efficiency indicated by the color of dots.

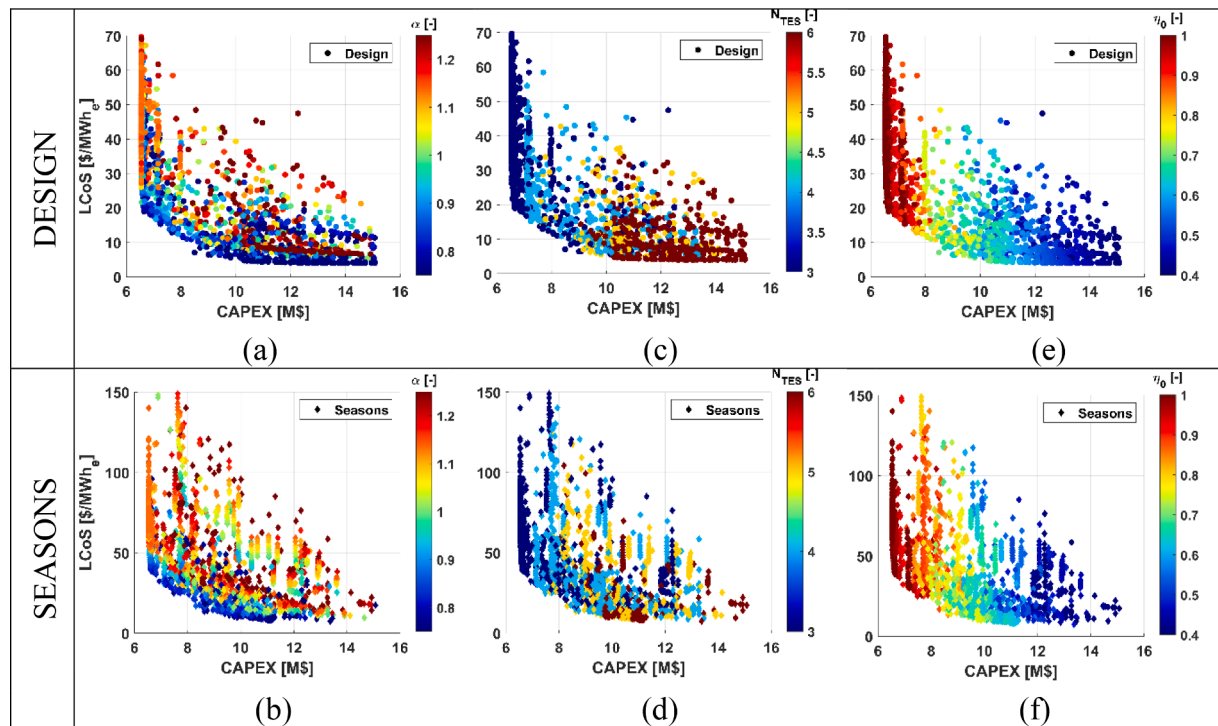


Fig. 11. LCoS versus CAPEX for MOO B, with color of dots given by aspect ratio for design (a) and seasonal (b) case. LCoS versus CAPEX for MOO B, with color of dots given by number of TES units for design (c) and seasonal (d) cases. LCoS versus CAPEX for MOO B, with color of dots given by preliminary efficiency for design (e) and seasonal (d) cases.

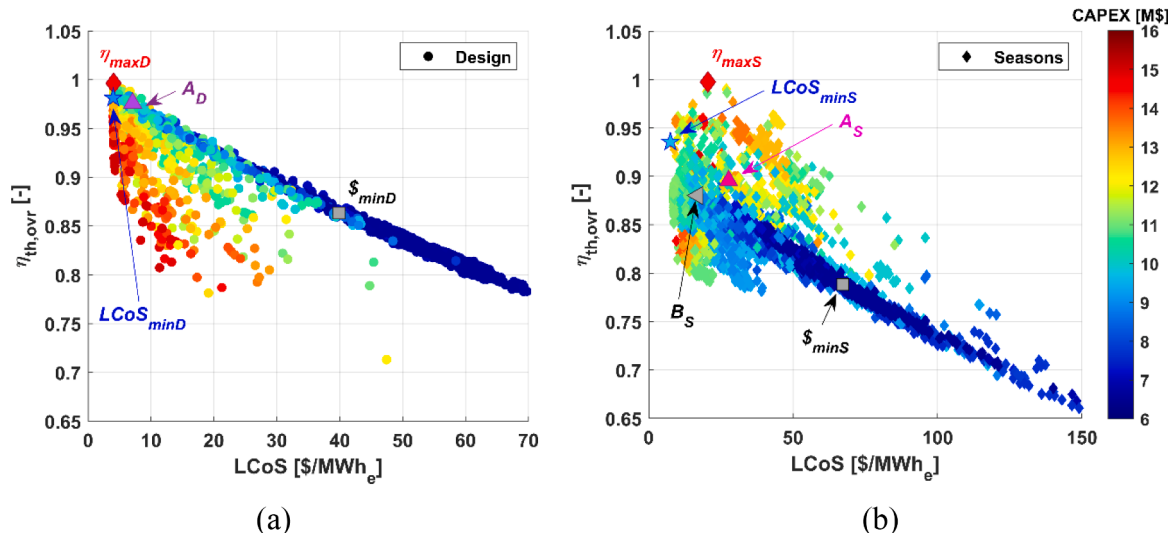


Fig. 12. (a) Multi-Objective Optimization C results, TES thermal efficiency versus LCoS under steady boundary conditions, with CAPEX indicated by the color of dots; (b) Multi-Objective Optimization C results, TES thermal efficiency versus LCoS under quasi-dynamic boundary conditions, with CAPEX indicated by the color of dot.

4.3. Multi-objective optimization: case B

Fig. 10 shows the results of the MO optimization B. The LCoS is plotted against the CAPEX for HTF mass flow rate design (Fig. 10(a)) and seasonal (Fig. 10(b)) profiles. The color of the dots represents the overall thermal efficiency of the TES. The corresponding Pareto frontiers are drawn and the design points identified in Tables 7 and 8 are also reported in Fig. 10. A clear trade-off between LCoS and CAPEX appears, indeed lower LCoS requires higher CAPEX. Along the Pareto frontiers, a reduction in the LCoS is related to an increase of the TES thermal

efficiency. Quasi-dynamic boundary conditions lead to higher LCoS (an average increase of about 88% for similar CAPEX), affected by the lower $\eta_{th,ovr}$, and a steeper Pareto front. Considering steady boundary conditions most of the TES design belonging to the Pareto curve identified in MOO A can be found also along the Pareto frontier of MOO B (i.e. points η_{maxD} and A_D in Fig. 10(a)). Contrarily, including quasi-dynamic boundary conditions the optimal TES designs identified during MOO A and MOO B do not overlap (except the ones at very low CAPEX, low $\eta_{th,ovr}$ and high LCoS). These results suggest that when optimizing packed bed TES both $\eta_{th,ovr}$ and LCoS should be considered.

In the context of MOO B, as shown in Fig. 11, the behavior of the objectives with respect to the decision variables for the optimal designs is relatively similar for both analyzed HTF mass flow rate scenarios. Under both steady and quasi-dynamic boundary conditions, a low α , between 0.75 and 0.8, is always preferred. A unitary aspect ratio ensures the maximum compactness, which leads to minimal costs. However, lower aspect ratio implies reduced pressure losses and worse thermal performance due to shorter TES and limited distance between cold and hot TES regions. In order to minimize the LCoS, a high number of TES units is always chosen. However, five or six TES units are considered only for the very right side part of the Pareto fronts, where large CAPEX increases lead to relatively small LCoS decreases. Similar trends can be identified also for the preliminary sizing efficiency. A reduction of η_0 enables lower LCoS, reaching the minimum LCoS for an η_0 of about 0.47 and 0.48 in the design and seasonal case, Fig. 11(e) and (f), respectively. An increasing particle diameter, from 0.06 m to 0.1 m, enable to minimize the LCoS for increasing CAPEX under both considered \dot{m}_{HTF} profiles. In order to explain these trends, it can be noted that more TES units, low aspect ratio and low initial efficiency means higher installation costs but also enhanced performance during operations. Specifically, decreased pressure drop and increased thermal losses toward the ambient, which are still limited thanks to an assumed thick high and low temperature insulation. Therefore, this leads to lower OPEX and energy cost for charging and discharging the TES, and higher energy production, which counteract the increase in the CAPEX resulting in lower LCoS.

4.4. Multi-objective optimization: case C

The results of the MOO C are reported in Fig. 12. The TES thermal efficiency, $\eta_{th,ovr}$, is plotted against the TES LCoS for HTF mass flow rate design (Fig. 12(a)) and seasonal (Fig. 12 (b)) profiles. In Fig. 12 the

selected points, $\$_{minD}$, $LCoS_{minD}$, η_{maxD} , A_D , $\$_{minS}$, $LCoS_{minS}$, η_{maxS} , A_S and B_S belonging to the Pareto curves identified in the previous MOOs are also shown. The average efficiency achievable in the design working condition case is more than 5% higher than the one achieved in the seasonal scenario. Under steady boundary conditions a linear relationship between LCoS and $\eta_{th,ovr}$ can be identified with increasing $\eta_{th,ovr}$ for decreasing LCoS. Most of the optimal TES designs identified during MOO A and MOO B lies along this linear trend between $\$_{minD}$ and η_{maxD} . Exceptions are the optimal design at very low LCoS, which are grouped at the peak of the design space (around $LCoS_{minD}$ and η_{maxD}). Including quasi-dynamic boundary conditions, a similar linear relationship between LCoS and $\eta_{th,ovr}$ can be identified for high LCoS, low $\eta_{th,ovr}$ and low CAPEX. For higher TES thermal efficiency and lower LCoS a larger spread of the TES design points can be described with respect to the design case.

Looking at the set of decision variables for the different TES design points in the context of MOO C, as shown in Fig. 13, different relationships for the two studied scenarios can be identified. Under steady boundary conditions, an increase of the particle diameter is required to enhance the TES thermal efficiency and minimize the LCoS. Under quasi-dynamic boundary conditions, Fig. 13(b), small d_p lead to enhanced $\eta_{th,ovr}$ while larger particle diameter enable reductions of the LCoS. This difference is explained by the greater relative importance of the pumping energy (and related OPEX), minimized at large d_p , in the LCoS. Finally, a high number of TES units is generally preferred. In the design case, shown in Fig. 13(c), six TES units are considered for the design at the lowest LCoS. Under quasi-dynamic boundary condition, Fig. 13(d), four to six TES units are considered in the design space at low LCoS and high $\eta_{th,ovr}$. Particularly, five TES units are preferred, in connection with small particle diameters, to increase $\eta_{th,ovr}$; while six TES unit are preferred together with large d_p to minimize the LCoS.

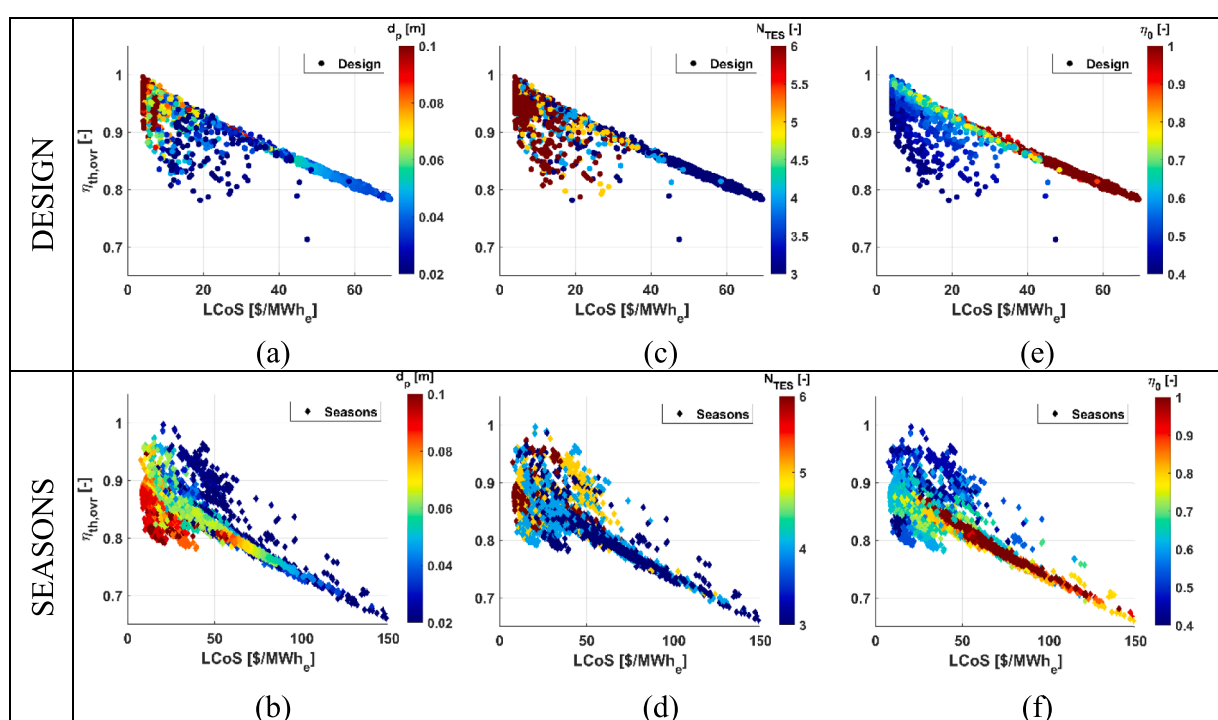


Fig. 13. TES thermal efficiency versus LCoS for MOO C, with color of dots given by particle diameter for design (a) and seasonal (b) case. TES thermal efficiency versus LCoS for MOO C, with color of dots given by number of TES units for design (c) and seasonal (d) cases. TES thermal efficiency versus LCoS for MOO C, with color of dots given by preliminary efficiency for design (e) and seasonal (f) cases.

5. Conclusions

In the present work, the thermo-economic performance of a packed bed TES has been studied and optimized. Additionally, the Levelized Cost of Storage (LCoS) concept has been innovatively applied to the TES concept. In doing so, a complete methodology to design packed bed TES has been outlined and proposed. As part of this methodology, a comprehensive multi-objective optimization of an industrial scale packed bed has been performed by means of an evolutionary genetic algorithm considering both steady and quasi-dynamic boundary conditions. The outcomes of this work show that:

- 1 Variable heat transfer fluid mass flow rate during charge widely affects the TES performance, both in terms of thermal efficiency and thermocline behavior. Quasi-dynamic boundary conditions lead to a reduction of about 5% in the TES thermal efficiency. The transient behavior of the boundary conditions should be considered when optimizing TES.
- 2 Analyzing only the TES overall thermal efficiency against the CAPEX, the final Pareto curves and the relative sets of optimal TES designs are strongly affected by quasi-dynamic boundary conditions.
- 3 The LCoS is negatively affected by quasi-dynamic boundary conditions. However, independently from the heat transfer fluid mass flow rate profile, similar influences of the design variables over the TES optimization are identified. Therefore, the LCoS could be considered as a more reliable performance indicator for packed bed TES, as less dependent on heat transfer fluid mass flow rate boundary conditions.
- 4 Maximal TES thermal efficiencies are achieved with aspect ratio between 0.75 and 0.9, medium to large particles and a high number of TES units.
- 5 Minimal LCoS requires bigger pebbles and preliminary efficiencies between 0.45 and 0.6 together with a high number of TES units.
- 6 Minimal CAPEX are attained with unitary aspect ratio and preliminary efficiency.

Future work will be focused on the introduction of the different optimal TES configurations gathered in this analysis into complete CSP plant models to understand which optimization strategy could lead to optimal TES design, not only at the component level, but also under a broader system perspective. Finally, the influence of other design parameters will be tested looking further into the correlations among them and the procedure will be applied to different TES sizes and geometries.

CRediT authorship contribution statement

Silvia Trevisan: Conceptualization, Methodology, Investigation, Validation, Resources, Writing – original draft, Visualization. **Yousra Jemmal:** Conceptualization, Methodology, Supervision. **Rafael Guedez:** Conceptualization, Methodology, Supervision. **Björn Laumert:** Supervision, Project administration, Funding acquisition.

Declaration of Competing Interest

The authors declare that they have no known competing financial interests or personal relationships that could have appeared to influence the work reported in this paper.

Acknowledgments

This research has been funded by the Swedish Energy Agency and Azelio AB through the Energy Agency program Electricity from the Sun, project P43284-1.

References

- [1] W.D. Steinmann, Thermal energy storage systems for concentrating solar power (CSP) plants, *Conc. Sol. Power Technol. Princ. Dev. Appl.* (2012) 362–394, <https://doi.org/10.1016/B978-1-84569-769-3.50011-X>.
- [2] EASE/EERA, European Energy Storage Technology Development Roadmap, 2017.
- [3] M. Mehos, C. Turchi, J. Vidal, M. Wagner, Z. Ma, C. Ho, et al., Concentrating Solar Power Gen3 Demonstration Roadmap, 2017.
- [4] G. Zanganeh, A. Pedretti, S. Zavattini, M. Barbato, A. Steinfeld, Packed-bed thermal storage for concentrated solar power - pilot-scale demonstration and industrial-scale design, *Sol. Energy* 86 (2012) 3084–3098, <https://doi.org/10.1016/j.solener.2012.07.019>.
- [5] M. Hänchen, S. Brückner, A. Steinfeld, High-temperature thermal storage using a packed bed of rocks - heat transfer analysis and experimental validation, *Appl. Therm. Eng.* (2011) 1798–1806, <https://doi.org/10.1016/j.apithermaleng.2010.10.034>.
- [6] G. Zanganeh, A. Pedretti, A. Haselbacher, A. Steinfeld, Design of packed bed thermal energy storage systems for high-temperature industrial process heat, *Appl. Energy* 137 (2015) 812–822, <https://doi.org/10.1016/j.apenergy.2014.07.110>.
- [7] I. González, C. David Pérez-Segarra, O. Lehmkühl, S. Torras, A. Oliva, Thermo-mechanical parametric analysis of packed-bed thermocline energy storage tanks, *Appl. Energy* 179 (2016) 1106–1122, <https://doi.org/10.1016/j.apenergy.2016.06.124>.
- [8] A.M. Bonanos, E.V. Votyakov, Sensitivity analysis for thermocline thermal storage tank design, *Renew. Energy* 99 (2016) 764–771, <https://doi.org/10.1016/j.renene.2016.07.052>.
- [9] H. Torab, D.E. Beasley, Optimization of a packed bed thermal energy storage unit, *J. Sol. Energy Eng.* 109 (1987) 170–175, <https://doi.org/10.1115/1.3268201>.
- [10] A.S.A. Ammar, A.A. Ghoneim, Optimization of a sensible heat storage unit packed with spheres of a local material, *Renew. Energy* 1 (1991) 91–95, [https://doi.org/10.1016/0960-1481\(91\)90107-Z](https://doi.org/10.1016/0960-1481(91)90107-Z).
- [11] O. Maaliou, B.J. McCoy, Optimization of thermal energy storage in packed columns, *Sol. Energy* 34 (1985) 35–41.
- [12] C. Lundgaard, K. Engelbrecht, O. Sigmund, A density-based topology optimization methodology for thermal energy storage systems, *Struct. Multidiscip. Optim.* 60 (2019) 2189–2204, <https://doi.org/10.1007/s00158-019-02375-8>.
- [13] C. Choudhury, P.M. Chauhan, H.P. Garg, Economic design of a rock bed storage device for storing solar thermal energy, *Sol. Energy* 55 (1995) 29–37, [https://doi.org/10.1016/0038-092X\(95\)00023-K](https://doi.org/10.1016/0038-092X(95)00023-K).
- [14] A.J. White, J.D. McTigue, C.N. Markides, Analysis and optimisation of packed-bed thermal reservoirs for electricity storage applications, *Proc. Inst. Mech. Eng. Part A J. Power Energy* (2016), <https://doi.org/10.1177/0957650916668447>.
- [15] J. Martí, L. Geissbühler, V. Becattini, A. Haselbacher, A. Steinfeld, Constrained multi-objective optimization of thermocline packed-bed thermal-energy storage, *Appl. Energy* 216 (2018) 694–708, <https://doi.org/10.1016/j.apenergy.2017.12.072>.
- [16] B. Cárdenas, T.R. Davenne, J. Wang, Y. Ding, Y. Jin, H. Chen, et al., Techno-economic optimization of a packed-bed for utility-scale energy storage, *Appl. Therm. Eng.* 153 (2019) 206–220, <https://doi.org/10.1016/j.apithermaleng.2019.02.134>.
- [17] Lazard, Lazard's Levelized Cost of Storage Analysis - version 4, 0, 2018.
- [18] I. Pawel, The cost of storage – how to calculate the levelized cost of stored energy (LCOE) and applications to renewable energy generation, *Energy Procedia* 46 (2014) 68–77, <https://doi.org/10.1016/j.egypro.2014.01.159>.
- [19] V. Jülich, Comparison of electricity storage options using levelized cost of storage (LCoS) method, *Appl. Energy* 183 (2016) 1594–1606, <https://doi.org/10.1016/j.apenergy.2016.08.165>.
- [20] A. Smallbone, V. Jülich, R. Wardle, A.P. Roskilly, Levelised cost of storage for pumped heat energy storage in comparison with other energy storage technologies, *Energy Convers. Manag.* 152 (2017) 221–228, <https://doi.org/10.1016/j.enconman.2017.09.047>.
- [21] C. Luerssen, O. Gandhi, T. Reindl, K.W.D. Cheong, C. Sekhar, Levelised Cost of Thermal Energy Storage and Battery Storage to Store Solar PV Energy for Cooling Purpose, 2019, pp. 1–10, <https://doi.org/10.18086/eurosun2018.04.09>.
- [22] O. Schmidt, S. Melchior, A. Hawkes, I. Staffell, Projecting the future levelized cost of electricity storage technologies, *Joule* 3 (2019) 81–100, <https://doi.org/10.1016/j.joule.2018.12.008>.
- [23] TEW. Schumann, Heat transfer: a liquid flowing through a porous prism, *J. Franklin Inst.* (1929), [https://doi.org/10.1016/S0016-0032\(29\)91186-8](https://doi.org/10.1016/S0016-0032(29)91186-8).
- [24] E.W. Lemmon, M.L. Huber, M.O. REFPROP McLinden, Reference Fluid Thermodynamic and Transport Properties Database, 2013.
- [25] R. Tiskatine, R. Oaddi, R. Aït El Cadi, A. Bazgaou, L. Bouirden, A. Aharoune, et al., Suitability and characteristics of rocks for sensible heat storage in CSP plants, *Sol. Energy Mater. Sol Cells* 169 (2017) 245–257, <https://doi.org/10.1016/j.solmat.2017.05.033>.
- [26] R. Tiskatine, A. Aharoune, L. Bouirden, A. Ihlal, Identification of suitable storage materials for solar thermal power plant using selection methodology, *Appl. Therm. Eng.* 117 (2017) 591–608, <https://doi.org/10.1016/j.apithermaleng.2017.01.107>.
- [27] V. Becattini, T. Motmans, A. Zappone, C. Madonna, A. Haselbacher, A. Steinfeld, Experimental investigation of the thermal and mechanical stability of rocks for high-temperature thermal-energy storage, *Appl. Energy* 203 (2017) 373–389, <https://doi.org/10.1016/j.apenergy.2017.06.025>.
- [28] R. Haenel, L. Rybach, L. Stegema, Handbook of Terrestrial Heat-Flow Density Determination: Guidelines and Recommendations of the International Heat Flow Commission, 1988, <https://doi.org/10.1007/978-94-009-2847-3>.

- [29] Weisstein E.W. Sphere Packing. MathWorld—A Wolfram Web Resour 2020. <https://mathworld.wolfram.com/SpherePacking.html>.
- [30] A. Meier, C. Winkler, D. Wuillemin, Experiment for modelling high temperature rock bed storage, Sol. Energy Mater. 24 (1991) 255–264, [https://doi.org/10.1016/0165-1633\(91\)90066-T](https://doi.org/10.1016/0165-1633(91)90066-T).
- [31] J. Beek, Design of packed catalytic reactors, Adv. Chem. Eng. (1962), [https://doi.org/10.1016/S0065-2377\(08\)60060-5](https://doi.org/10.1016/S0065-2377(08)60060-5).
- [32] T.L. Bergman, A.S. Lavine, F.P. Incropera, D.P. Dewitt, Fundamentals of Heat and Mass Transfer - Seventh Edition, 2001.
- [33] J.P. Coutier, E.A. Farber, Two applications of a numerical approach of heat transfer process within rock beds, Sol. Energy 29 (1982) 451–462, [https://doi.org/10.1016/0038-092X\(82\)90053-6](https://doi.org/10.1016/0038-092X(82)90053-6).
- [34] B. Stuke, Berechnung des Wärmeaustausches in Regeneratoren mit zylindrischen und kugelförmigen Füllmaterial, Angew Chemie 20 (1948) 262–268, <https://doi.org/10.1002/ange.19480201004>.
- [35] B. Xu, P.W. Li, C.L. Chan, Extending the validity of lumped capacitance method for large Biot number in thermal storage application, Sol. Energy 86 (2012) 1709–1724, <https://doi.org/10.1016/j.solener.2012.03.016>.
- [36] D. Kunii, J.M. Smith, Heat transfer characteristics of porous rocks, AIChE J. 6 (1960) 71–78, <https://doi.org/10.1002/aic.690060115>.
- [37] P. Cheng, C.-T. Hsu, Heat Conduction, Transp. Phenom. Porous Media, Pergamon, 1998, pp. 57–76, <https://doi.org/10.1016/B978-0-08-042843-7.50003-9>.
- [38] S. Ergun, A.A. Orning, Fluid flow through randomly packed columns and fluidized beds, Ind. Eng. Chem. 41 (1949) 1179–1184, <https://doi.org/10.1021/ie50474a011>.
- [39] NREL, SAM, CSP Models - System Advisor Model (SAM) (2018).
- [40] C. Kost, S. Shammugam, V. Jülich, H.-T. Nguyen, T. Schlegl, Levelized Cost of Electricity Renewable Energy Technologies, 2018.
- [41] MATLAB, Multiobjective optimization 2019, <https://se.mathworks.com/discovery/multiobjective-optimization.html> (accessed June 24, 2019).
- [42] MATLAB, Optimization toolbox 2019, <https://se.mathworks.com/products/optimization.html> (accessed June 24, 2019).
- [43] MathWorks, gamultiobj n.d. <https://se.mathworks.com/help/gads/gamultiobj.html> (accessed June 24, 2019).
- [44] JS. Arora, Genetic algorithms for optimum design, Introd. Optim. Des. (2012) 643–655, <https://doi.org/10.1016/b978-0-12-381375-6.00016-4>.